Lawrence Berkeley Laboratory
UNIVERSITY OF CALIFORNIA

Presented at the IEEE Symposium on Nuclear Science, Kissimmee, FL, November 11, 1988, and to be published in the Proceedings

Compensation for Crystal Penetration in High Resolution Positron Tomography

R.H. Huesman, E.M. Salmeron, and J.R. Baker

November 1988

Donner
Biology & Medicine Division

Prepared for the U.S. Department of Energy under Contract Number DE-AC03-76SF00098.

DISCLAIMER

LBL-26308

Compensation for Crystal Penetration in High Resolution Positron Tomography

Ronald H. Huesman, Eva M. Salmeron, and John R. Baker

Research Medicine and Radiation Biophysics Division
Lawrence Berkeley Laboratory
1 Cyclotron Road
Berkeley, California 94720
USA

Compensation for Crystal Penetration in High Resolution Positron Tomography

Ronald H. Huesman, Eva M. Salmeron, John R. Baker
Donner Laboratory and Lawrence Berkeley Laboratory
University of California, Berkeley, CA 94720

Abstract

We have characterized the effects of crystal penetration by annihilation photons in circular ring positron tomographs. They are most serious in high resolution instruments having small detectors. When annihilation photons are not normally incident and penetrate some distance into the scintillator before interacting, the measurement of their transverse position becomes uncertain. This penetration of photons into the detector material before interaction is a statistical process which leads to significant displacement and anisotropy of the point spread function. The subject of this work is mathematical correction of emission datasets by performing a two-dimensional spatially variant deconvolution of the emission data in sinogram format. Examples for the Donner 600-Crystal Positron Tomograph are presented, and the amplification of statistical errors resulting from the correction procedure is also discussed.

1 Introduction

The detection of annihilation photons in positron tomography is often performed with a scintillating material surrounding the transverse section. In our PET designs, individual scintillation crystals form a ring around the transverse section, each crystal being coupled to a photomultiplier tube. This ring of crystals is tightly packed to form an annulus.

When annihilation photons are not normally incident and penetrate some distance into the scintillator before interacting, the measurement of their transverse position becomes uncertain. This happens because the photon can pass obliquely through a crystal and enter the neighboring crystal before interacting. The effect is more pronounced with high resolution tomographs which have very small crystals, such as the Donner 600-Crystal Positron Tomograph and causes radial blurring that increases with distance from the center of the tomograph, as shown in figure 1. Although the subject of this work is mathematical compensation for crystal penetration, active research to measure the depth of interaction in the detectors is also underway. [1]

Figure 2 illustrates penetration of non-normally incident annihilation photons into the detector material before interaction. We assume here that the detectors have very good resolution but that they can measure the interaction point of the photons only in the azimuthal direction. The solid vertical line represents the path of two opposing annihilation photons. It is usually assumed that these photons have been detected at the inner face of the scintillation crystals. Since the photons penetrate some distance into the crystals before interacting, the measured interaction point of a photon is the projection of the actual interaction point onto the inner crystal surface. This effect tends to shift the measured path of the annihilation photons toward the center of the tomograph, usually with a change in angle. The vertical grey stripe on figure 2 represents the envelope of measured chords.

From the detection geometry, it can be seen that the effects of crystal penetration are more pronounced for actual chords which are further from the center of the tomograph.

2 Correction for physical effects

It is well known that undesireable physical effects in the data acquisition process can be most easily compensated for by using optimization methods to perform tomographic image reconstruction. These optimization methods are generally implemented as iterative algorithms, and the statistical properties of the resulting images are difficult to characterize.

Conversely, *direct* image reconstruction methods are based on analytic inversion formulas and are usually at least an order of magnitude faster than iterative algorithms. Direct methods are implemented as linear algorithms, and statistical analysis is straightforward, but physical effects can be difficult to incorporate. If kinetic analysis and compartmental modeling of sequential sets of images are to be performed, the statistical properties of images can be used to calculate error bounds on the model parameters. [2]

*This work was supported by the Office of Energy Research, Office of Health and Environmental Research, of the U.S. Department of Energy under contract No DE-AC03-76SF00098.

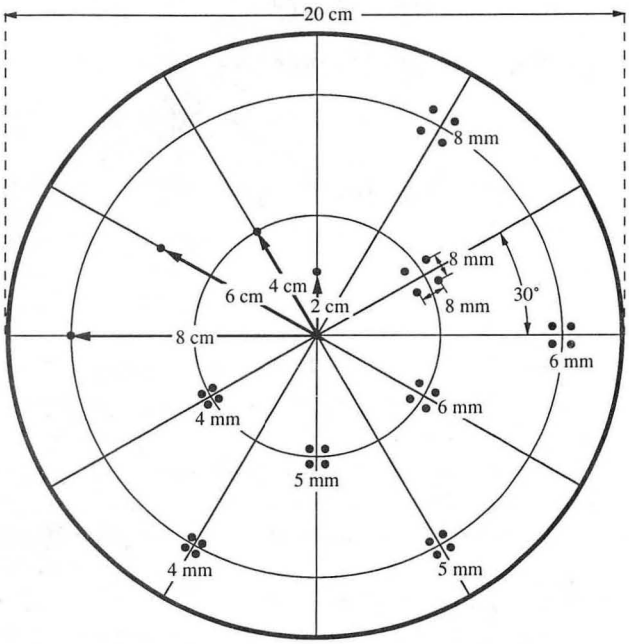

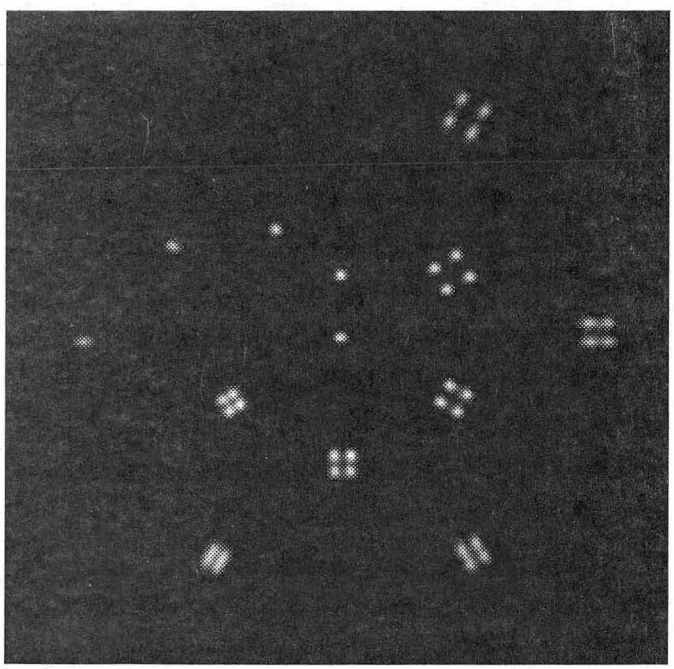

Figure 1: a) Upper, schematic diagram of a phantom with 37 line sources in a 20 cm diameter cylinder of lucite. b) Lower, reconstructed image (backprojection of filtered projections) of 37 point hot spot phantom data taken with the Donner 600-Crystal Positron Tomograph.

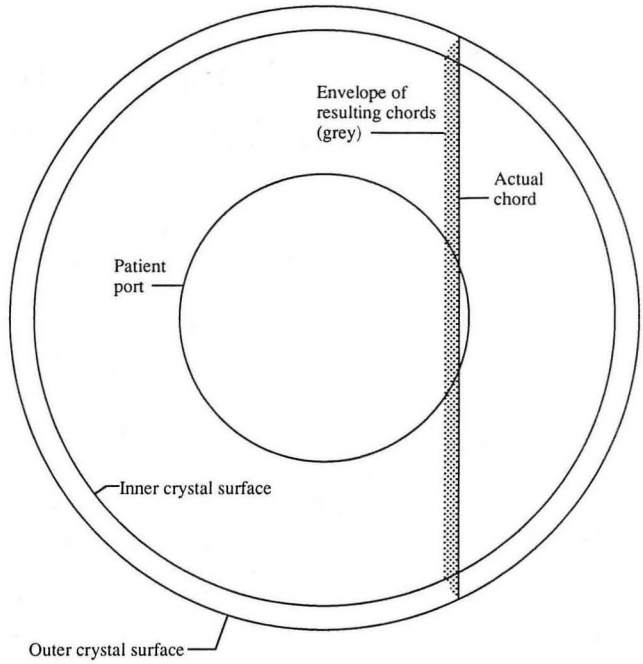

Figure 2: Effects of crystal penetration in an ideal ring.

In what follows we assume that the *ideal* PET data acquisition process is represented by

$$\langle \boldsymbol{p} \rangle = F\boldsymbol{f} \tag{1}$$

where $\boldsymbol{f}$ is a vector representing the distribution of radionuclide in the imaging plane, $\boldsymbol{p}$ is a vector representing the measured data with $\langle \boldsymbol{p} \rangle$ its expectation, and F is a matrix operator representing the ideal data acquisition process. The direct reconstruction algorithm is represented by

$$\hat{\boldsymbol{f}} = D\boldsymbol{p}^* \tag{2}$$

where $\boldsymbol{p}^*$ are measured data, $\hat{\boldsymbol{f}}$ is our estimate of the radionuclide distribution and D is a matrix.

There are two classes of physical effects in PET that can be easily accomodate by direct methods. [3] The first of these (denoted by the matrix operator H) can be interpreted as a modification of the source distribution before an ideal experiment; e.g., radioactive decay and the positron range effect. The second class of effects (denoted by the matrix operator G) can be interpreted as modifying the dataset from an ideal experiment; e.g., attenuation, intercrystal scatter, crystal penetration, and instrumental effects such as detection efficiency and dead-time. For these two classes of physical effects the non-ideal PET data acquisition process is represented by

$$\langle \boldsymbol{p} \rangle = G[F(H\boldsymbol{f})] \tag{3}$$

and if the matrices G and H are invertible, the radionuclide distribution is estimated as

$$\hat{\boldsymbol{f}} = H^{-1}[D(G^{-1}\boldsymbol{p}^*)] \tag{4}$$

Since crystal penetration can be modeled by G, the goal of this work is to generate the sinogram blurring matrix, G, and its inverse G^{-1} and apply it to the acquired sinogram dataset as follows

$$\hat{\boldsymbol{p}} = G^{-1}\boldsymbol{p}^* \tag{5}$$

Then, the reconstructed image corrected for crystal penetration is given by

$$\hat{\boldsymbol{f}} = D\hat{\boldsymbol{p}} \tag{6}$$

and the covariance matrix of the estimate is given by

$$\begin{aligned} cov(\hat{\boldsymbol{f}}) &= Dcov(\hat{\boldsymbol{p}})D^T & (7)\\ &= DG^{-1}cov(\boldsymbol{p}^*)(G^{-1})^T D^T & (8) \end{aligned}$$

where

$$cov(\hat{\boldsymbol{p}}) = G^{-1}cov(\boldsymbol{p}^*)(G^{-1})^T \tag{9}$$

In what follows, we shall reconstruct dataset with enough events that statistical fluctuations will not be evident and any artifacts will be due to the correction procedure. The reconstruction method used is backprojection of filtered projections [4], and a ramp filter is used without smoothing.

3 Methods

An acquired dataset may be visualized by presenting it as a sinogram (a two-dimensional array of histogram bins corresponding to pairs of crystals of the tomograph). Vertical position on the sinogram represents the the angle of the paths of annihilation photons, and the horizontal position represents distance from the center of the tomograph. Figure 3 shows a single chord of angle θ and distance z from the center. On the left is a drawing of a tomograph of 32 detectors, and on the right is a sinogram showing diamond shaped bins which correspond to chords passing through the front faces of pairs of crystals. The sinogram bin filled with gray is the bin in which the single chord falls. Projection angles, θ, range from $-90°$ to $+90°$ in this sinogram format and z takes on both positive and negative values.

3.1 Monte Carlo simulation of data

We define ideal PET data as having been acquired by a circular ring tomograph where the annihilation photons interact at the front face of the detectors. The effect of crystal penetration is studied by comparing ideal data with data where annihilation photons penetrate into the crystals before interacting. The depth of interaction is governed by an exponential distribution with an attenuation coefficient equal to 1.0 cm^{-1}. This is an approximate number for 511 keV photons in BGO, and we have

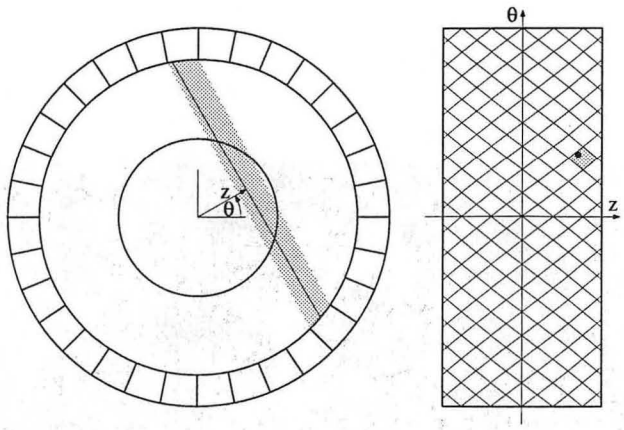

Figure 3: Representation of a sinogram element in the tomograph.

simplified the physical model such that an incident photon interacts exactly once in the detectors (as if the total cross-section were due only to photoelectric interactions).

We have performed Monte Carlo simulations of crystal penetration using the geometry of the Donner 600-Crystal Positron Tomograph in the *clam shut* mode (or position). This device is comprised of a 600 close-packed 3 mm wide BGO crystals in a circular ring of diameter 60 cm. The average depth of the crystals is 25 mm, and the patient port is 30 cm in diameter. [5] The character of the results of these simulations is shown in Figure 4 for crystals with and without penetration.

3.2 Generation of the penetration matrix G

In order to post correct data for crystal penetration, we need the transition probabilities which would transform an ideal dataset into one with penetration. The sinogram blurring matrix can be created from Monte Carlo simulations or evaluated from closed form integrals with the geometric and physical characteristics described above. For Monte Carlo simulations, each of the following is repeated many times to improve the statistical quality of the matrix estimate;

1. generate randomly a position at the face of the two crystals composing the *ideal* chord,
2. calculate the actual chord formed,
3. let this chord penetrate into each crystal with a random depth selected from the exponential distribution described above, and
4. histogram an event for the new pair of crystals corresponding to the *blurred* chord.

The results given in this paper were derived from the generation of one million Monte Carlo events per chord. Examples of the transition probabilities in the blurring

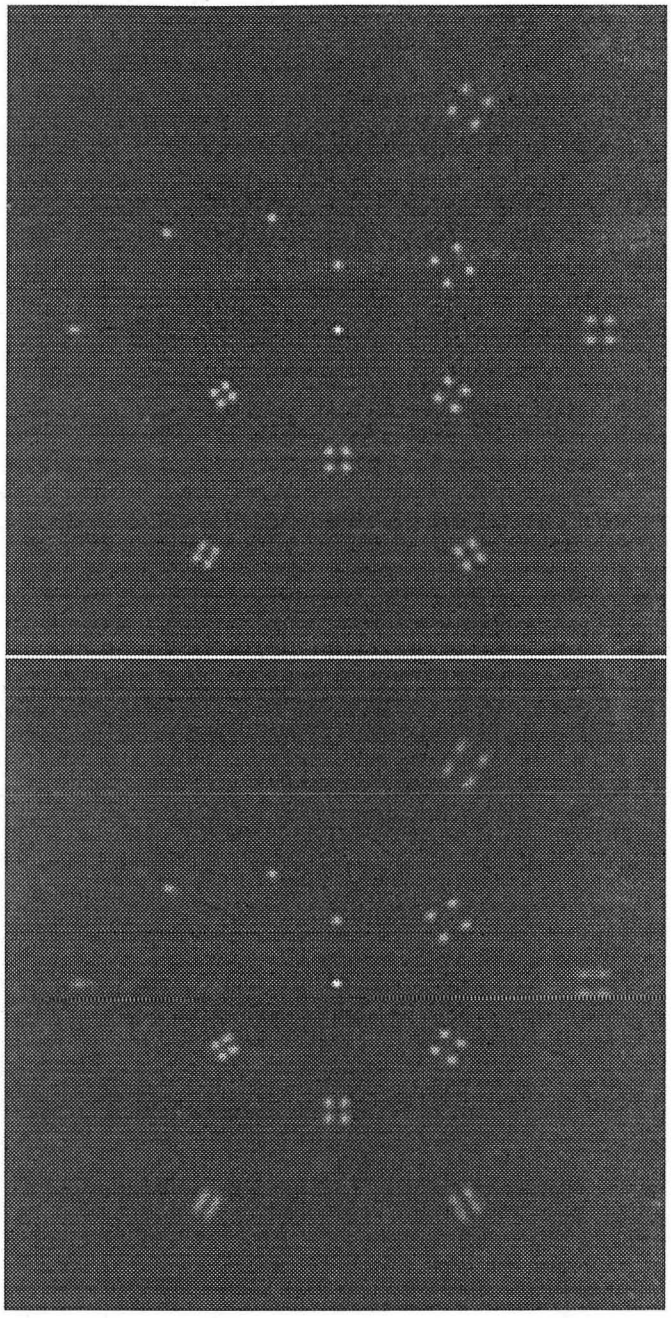

Figure 4: Reconstructed images (backprojection of filtered projections) of Monte Carlo penetration simulations for 37 point hot spot phantom. a) Upper, without penetration b) Lower, with penetration.

.0		.017		.0
	.013		.232	
.001		.189		.284
	.013		.232	
.0		.017		.0

Table 1: Matrix elements in sinogram format for chords 6 cm from the center of the Donner 600-Crystal Positron Tomograph. The value in the small box is the diagonal element, and the center of the tomograph is to the left.

.0		.001		.0		.0
	.001		.002		.0	
.0		.028		.062		.0
	.013		.078		.135	
.005		.036		.170		.107
	.013		.078		.135	
.0		.028		.062		.0
	.001		.002		.0	
.0		.001		.0		.0

Table 2: Matrix elements in sinogram format for chords 12 cm from the center of the Donner 600-Crystal Positron Tomograph. The value in the small box is the diagonal element, and the center of the tomograph is to the left.

matrix are given in tables 1 and 2 for ideal chords at 6 cm and 12 cm from the center of the tomograph, respectively. The diagonal elements of the matrix are in the small rectangles. The values in these tables are transition probabilities of the average ideal chord being transferred to another sinogram bin closer to the center of the tomograph. In both tables, bins closer to the center of the tomograph are on the left.

3.3 Matrix structure

Notice that the number of different probability values in the blurring matrix is limited due to rotational symmetry. Transition probabilities from sinogram bins the same distance from the center have the same description but with a rotation on resulting chords, so that respective columns of the matrix are permutations of one another. Thus, it is possible to construct a circulant block matrix G [6].

Circulant block for G is obtained by arranging the elements of the data vector, $\boldsymbol{p}$, in blocks according to distance from the center of the tomograph and by ordering the elements within each block according to angle. Furthermore, since the transition matrix only moves chords close to the center, arranging the blocks of $\boldsymbol{p}$ in order of decreasing distance from the center makes the matrix lower triangular. The structure of the matrix and blocks

is illustrated in equations 10 and 11.

The high resolution Donner 600-Crystal Positron Tomograph puts each crystal in coincidence with 201 crystals on the opposite side of the ring leading to 201 radial sampling positions in *clam shut* mode and 200 radial samples in *clam open* position. The two corresponding matrices have dimension of 60300^2 and 60200^2, respectively. But, for the shut position, for example, a buffer of dimension $L = 101$ is sufficient for the diagonal scalars, and only $N = 5050$ buffers of dimension $M = 600$ are used for the non-zero circulant blocks of G, so $(5050 \times 600) + 101$ real values define the transition matrix.

$$G = \begin{bmatrix} G^{11} & 0 & .. & 0 \\ G^{21} & G^{22} & \ddots & \vdots \\ \vdots & \ddots & \ddots & 0 \\ G^{M1} & G^{M2} & .. & G^{MM} \end{bmatrix} \tag{10}$$

$$G^{kl} = \begin{bmatrix} g_1^{kl} & g_2^{kl} & g_3^{kl} & .. & g_{L-1}^{kl} & g_L^{kl} \\ g_L^{kl} & g_1^{kl} & g_2^{kl} & .. & g_{L-2}^{kl} & g_{L-1}^{kl} \\ g_{L-1}^{kl} & g_L^{kl} & g_1^{kl} & .. & g_{L-3}^{kl} & g_{L-2}^{kl} \\ \vdots & \vdots & \vdots & \ddots & \vdots & \vdots \\ g_3^{kl} & g_4^{kl} & g_5^{kl} & .. & g_1^{kl} & g_2^{kl} \\ g_2^{kl} & g_3^{kl} & g_4^{kl} & .. & g_L^{kl} & g_1^{kl} \end{bmatrix} \tag{11}$$

3.4 Matrix inversion

It can be shown that G is an invertible matrix (the diagonal elements are all non-zero), so a corrected sinogram can be obtained by calculating G^{-1} and multiplying it by the acquired sinogram. We choose to compute and apply matrix inverses rather than using back substitution [7] because the circulant block properties [6] of G can be used to improve the speed of the computation and G^{-1} is useful for covariance calculations [2].

The inverse is found by solving

$$G^{-1}G = I, \tag{12}$$

where I is the *identity* matrix. Let G^{kl} be the block elements of G and g_{ij}^{kl} be the elements of block G^{kl}. Similarly, let B^{kl} be the block elements of G^{-1} and b_{ij}^{kl} be the elements of block B^{kl}. Since G^{kl} and B^{kl} are circulant blocks, only b_{1j}^{kl} needs to be calculated (see the Appendix).

$$b_{jj}^{kk} = \frac{1}{g_{11}^{kk}} \tag{13}$$

$$b_{1j}^{kl} = -b_{11}^{ll}\left[b_{11}^{kk} g_{1j}^{kl} + \sum_{n=l+1}^{k-1}\left(\sum_{m=1}^{M} b_{1m}^{kn} g_{1(j-m+1) \bmod M}^{kl}\right)\right] \tag{14}$$

For a faster computation of the inverse, we can work with the discrete Fourier transform of the rows of the G^{kl} and B^{kl}. The inner sum in the Equation 14, $\sum_{m=1}^{M} b_j^{kn} g_{m-j+1}^{nl}$, is the periodic convolution of the two matrices G^{kl} and B^{kl}. In Fourier space a convolution becomes a multiplication; i.e., the Fourier transform diagonalizes G^{kl} and B^{kl}. If $\mathcal{G}^{kl}$ is the vector Fourier transform of the row representing G^{kl}, and $\mathcal{B}_{kl}$ of B^{kl}, α_{ij}^{kl}, and β_{ij}^{kl} their respective elements,

$$\mathcal{B}_{kl} = -b_{11}^{ll}\left(b_{11}^{kk}\mathcal{G}^{kl} + \sum_{n=l+1}^{k-1} \mathcal{B}_{kn}\mathcal{G}^{nl}\right) \tag{15}$$

and

$$\beta_{1j}^{kl} = -b_{11}^{kk}\left[b_{11}^{ll}\alpha_{1j}^{kl} + \sum_{n=l+1}^{k-1}\left(\beta_{1j}^{kn}\alpha_{1j}^{nl}\right)\right] \tag{16}$$

This can save a lot of time computing when calculating the inverse of G, if a fast Fourier transform (FFT) of the G^{kl} and B^{kl} is performed. That speedup depends on n, the length of the vector to transform; good FFT algorithms exist for n being a power of 2, for even number n, and for n a product of prime numbers, so it is possible to perform an FFT for any n. But tests show that in Donner PET case for the 600 crystal matrix the Fourier transform is very interesting, and not really time saving for the 601 crystal case (unfortunately, 601 is prime). FFTs can also be used to multiply the inverse matrix and sinogram.

4 Results

Figure 5 shows a reconstruction performed using the new correction procedure on simulated data for the 37 point hot spot phantom. Points that are on the outer edge are clearly improved over those reconstructed without correction shown in figure 4b.

Also visible in figure 5 however, are artifacts due to the correction procedure. These artifacts arise from the fact that the Monte Carlo simulation of this phantom used point sources. The matrix, G, has elements which are the *average* transition probability over the diamond-shaped sinogram bins shown in figure 3. Chords passing through an ideal point source fall on a sine wave in the sinogram, and the local path of the sine wave through a sinogram diamond will have different transition probabilities than the average over that diamond.

The deblurring procedure can cause substantial amplification of the statistical noise present in the emission data. Equation 9 describes the error propagation of the proposed restoration technique when the error of the data measurement process is known. Figure 6 shows the statistical uncertainty (square root of the variance) for corrected projection values when the emission dataset is assumed to be homoscedastic with unit variance; i.e., $cov(\boldsymbol{p}^*) = I$. We see that the error propagation becomes very large for chords far from the center. Figures 7 and 8 show two columns of the correlation matrix for projection chords that are 6 cm and 12 cm, respectively, from

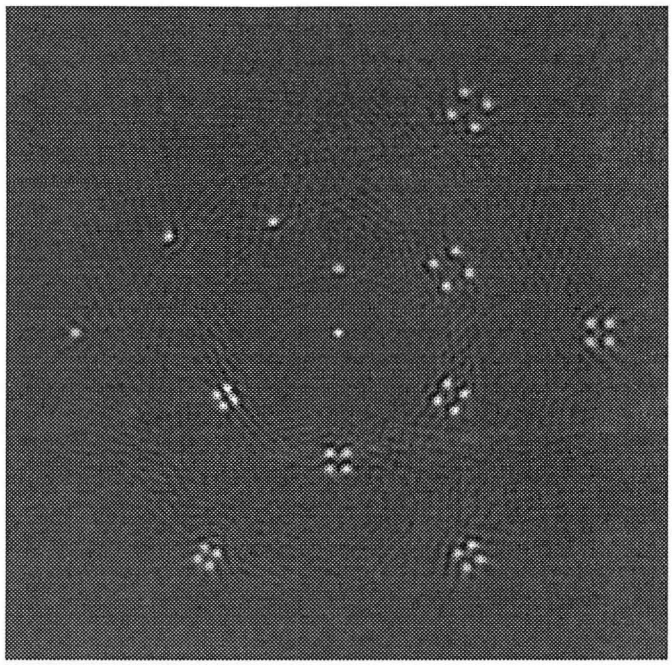

Figure 5: Reconstructed image (correction of sinogram with new method before backprojection of filtered projections) of Monte Carlo penetration simulation for 37 point hot spot phantom.

the center of the tomograph when the emission dataset is assumed to homoscedastic. Figures 6 through 8 have assumed each measured projection value to be independent and to have equal uncertainty; however, this is not necessarily true for real data.

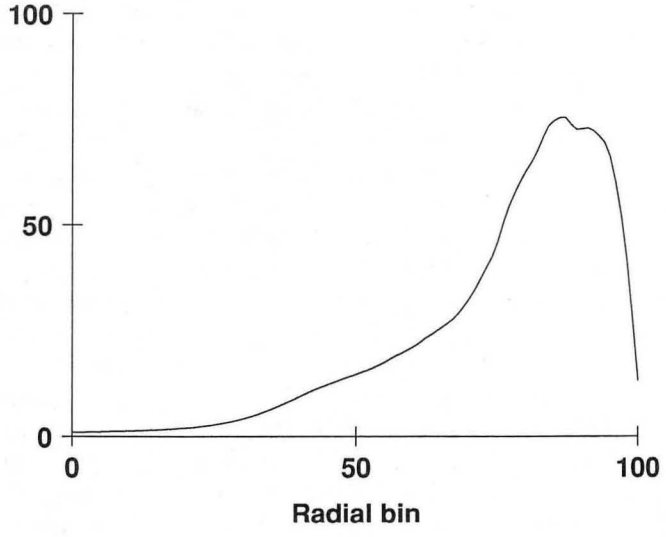

Figure 6: Projection standard deviation for chords that have been corrected with the new method vs. distance from the center of the Donner 600-Crystal Positron Tomograph.

The new correction procedure was applied to the same Donner 600-Crystal Positron Tomograph emission data

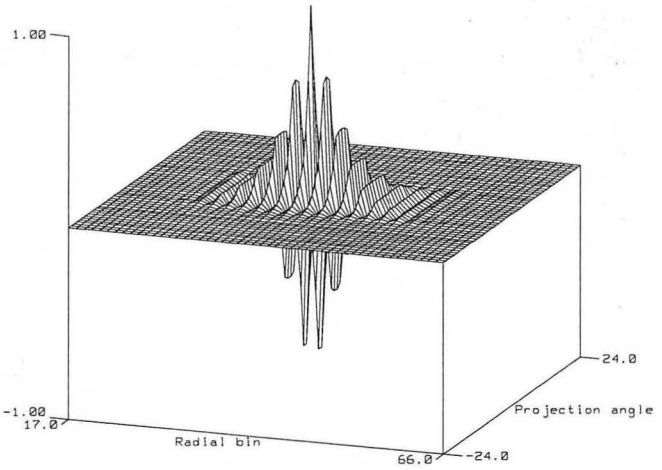

Figure 7: Projection correlation values in sinogram format for chords 6 cm from the center of the Donner 600-Crystal Positron Tomograph that have been corrected with the new method.

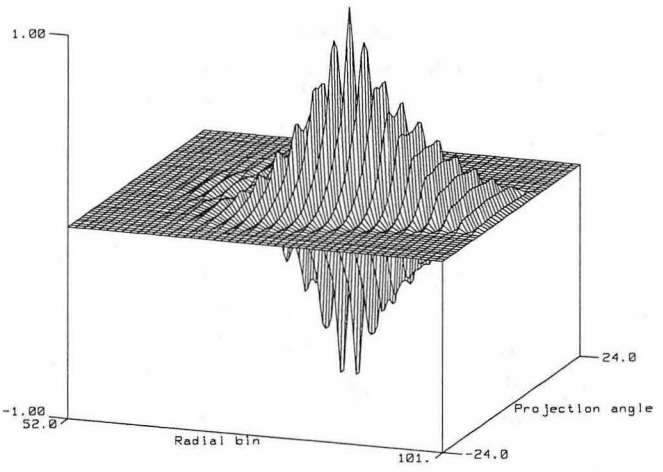

Figure 8: Projection correlation values in sinogram format for chords 12 cm from the center of the Donner 600-Crystal Positron Tomograph that have been corrected with the new method.

used in figure 1 and the resulting image is shown in figure 9. We notice here the same type of artifacts that are present in figure 5, except to a lesser extent.

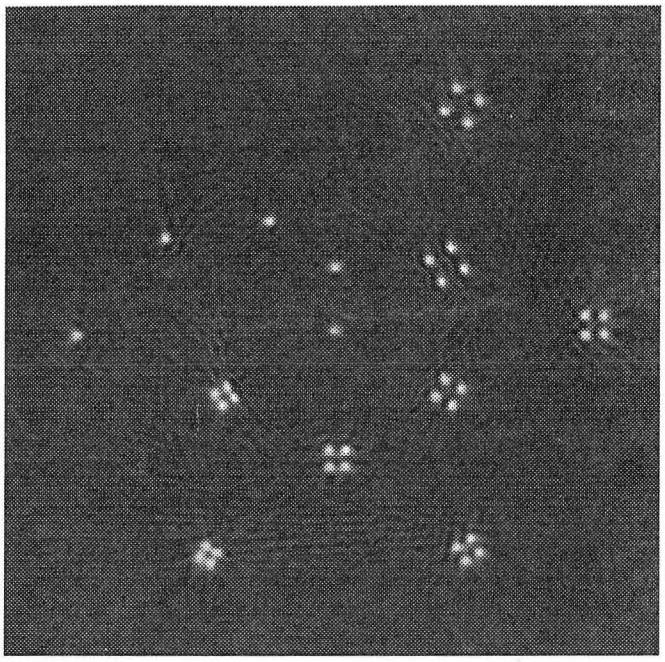

Figure 9: Reconstructed image (correction of sinogram with new method before backprojection of filtered projections) of 37 point hot spot phantom data taken with the Donner 600-Crystal Positron Tomograph.

5 Conclusions

We have developed a new method of compensating for crystal penetration by performing a two-dimensional, spatially variant deconvolution on the emission dataset. The method appears to amplify statistical noise a great deal in order to gain a modest improvement in radial resolution. The statistical correlations in the corrected projections are so high that images resulting from statistically poor data are expected to have a high degree of correlated noise.

Preliminary tests indicate that the method causes artifacts for data generated from point sources, because the assumptions made when the blurring transition probabilities were calculated are not met. Indeed, in other studies not reported here, the blurring matrix faithfully predicts the effect of crystal penetration when a point source is replaced by a Gaussian distribution with standard deviation equal to the radial sampling of the tomograph.

6 Acknowledgements

The authors would like to thank T F Budinger and R Marr for helpful discussions. This work was supported by the Office of Energy Research, Office of Health and Environmental Research, of the U.S. Department of Energy under contract No DE-AC03-76SF00098, by the National Institute of Health, National Heart, Lung, and Blood Institute under grants No HL07367 and HL25840, National Institute of Aging under grant AG05890, National Cancer Institute under grant CA38086, by La Fondation pour la Recherche Médicale, by Cray Research Inc., and by IBM Inc.

References

[1] Derenzo SE, WW Moses, HG Jackson, BT Turko, JL Cahoon, A Geyer, DC Uber, and T Vuletich. Initial characterization of a position-sensitive photodiode/BGO detector for pet. *IEEE Trans Nucl Sci*, **NS-36**, 1989. Submitted.

[2] Huesman RH and BM Mazoyer. Kinetic data analysis with a noisy input function. *Phys Med Biol*, **32**(12):1569–1579, 1987.

[3] Mazoyer BM, MS Roos, and RH Huesman. Dead time correction and counting statistics for positron tomography. *Phys Med Biol*, **30**:385–399, 1985.

[4] Ramachandran GN and AV Lakshminarayanan. In *Proc Natl Acad Sci US*, pages 2236–2240, 1971.

[5] Derenzo SE, RH Huesman, JL Cahoon, A Geyer, DC Uber, T Vuletich, and TF Budinger. Initial results from the Donner 600-crystal tomograph. *IEEE Trans Nucl Sci*, **NS-34**(1):321–325, 1987.

[6] Davis PJ. *Circulant Matrices. Pure and Applied Mathematics*, John Wiley and Sons, New York, NY, 1979.

[7] Strang G. *Linear Algebra and Its Applications.* Academic Press, Orlando, FL, 1980.

7 Appendix

With G^{kl} being the block elements of G, B^{kl} the corresponding block elements of G^{-1}, I^{kl} the same for I, and N the number of blocks in a row, we can write

$$I^{kl} = \sum_{n=1}^{N} B^{kn} G^{nl} \tag{17}$$

G^{-1} is a lower triangular matrix as G, then with $k \geq l$

$$I^{kl} = \sum_{n=l}^{k} B^{kn} G^{nl} \tag{18}$$

or

$$I^{kl} = B^{kl} G^{ll} + \sum_{n=l+1}^{k} B^{kn} G^{nl} \tag{19}$$

then

$$I^{kk} = B^{kk} G^{kk} \tag{20}$$

or

$$B^{kk} = (G^{kk})^{-1} \tag{21}$$

As the blocks G^{kk} are in fact $g_{11}^{kk} I^{kk}$ then

$$B^{kk} = \frac{1}{g_{11}^{kk}} I^{kk} \tag{22}$$

we can write

$$B^{kk} = \frac{1}{g_{11}^{kk}} I^{kk} = b_{11}^{kk} I^{kk} \tag{23}$$

and with $k \neq l$

$$B^{kl} G^{ll} + \sum_{n=l+1}^{k} B^{kn} G^{nl} = 0 \tag{24}$$

or

$$B^{kl} = -(G^{ll})^{-1} \sum_{n=l+1}^{k} B^{kn} G^{nl} \tag{25}$$

compute as

$$B^{kl} = -b_{11}^{ll} \left(b_{11}^{kk} G^{kl} + \sum_{n=l+1}^{k-1} B^{kn} G^{nl} \right) \tag{26}$$

The b_{ij}^{kl} elements of B^{kl} must now be computed for $k \neq l$, M is the row dimension of all B^{kl}, G^{kl} blocks $(k > n, n > l)$

$$b_{ij}^{kl} = -b_{11}^{ll} \left[b_{11}^{kk} g_{ij}^{kl} + \sum_{n=l+1}^{k-1} \left(\sum_{m=1}^{M} b_{in}^{kn} g_{nj}^{nl} \right) \right] \tag{27}$$

G^{kl} and B^{kl} are circulant blocks so we only need to calculate b_{1j}^{kl}

$$b_{1j}^{kl} = -b_{11}^{ll} \left[b_{11}^{kk} g_{1j}^{kl} + \sum_{n=l+1}^{k-1} \left(\sum_{m=1}^{M} b_{1k}^{kn} g_{1(j-m+1) \bmod M}^{nl} \right) \right] \tag{28}$$

LAWRENCE BERKELEY LABORATORY
TECHNICAL INFORMATION DEPARTMENT
UNIVERSITY OF CALIFORNIA
BERKELEY, CALIFORNIA 94720